(Received 9 February 2026, Accepted 27 March 2026, Scheduled 6 April 2026)

Multiobjective Optimization of Insulation Structure for Converter Transformer Valve-Side Bushings

Da Xie[1], Wei Wang[1], Yongchao Li[2,*], Siyi Wei[1], Gang Xu[1], and Long Ma[2]

[1] *Guangdong Power Grid Co., Ltd., Guangdong, China*
[2] *2School of Electrical and Electronic Enginnering, North China Electric Power University, Baoding, China*

ABSTRACT: Valve-side bushings in HVDC converter transformers operate under composite AC-DC electric stresses, where temperature-dependent conductivity induces significant redistribution of electric field. In this study, a unified electro-thermal coupled model is developed for a 226 kV capacitive grading structure. Two insulation margin indices corresponding to DC lifetime stress and AC partial discharge stress are defined, and a multiobjective optimization model is formulated to minimize the normalized variances of both margins. An improved multiobjective grey wolf optimizer with a nonlinear convergence factor and a crowding-solution screening mechanism is proposed to enhance convergence and Pareto-solution quality. Results show that the improved algorithm yields better Pareto-solution diversity and uniformity than the standard method, while the optimized structure reduces the maximum DC and AC electric fields by about 6.2% and 10.4%, respectively. The proposed method provides an effective design approach for improving insulation coordination and reliability of valve-side bushings under composite AC-DC stresses.

1. INTRODUCTION

In high-voltage direct current (HVDC) transmission systems, the valve-side bushing of a converter transformer serves as the electrical interface between the converter valve and transformer, and is therefore a critical component in practical engineering applications [1, 2]. Under actual operating conditions, a valve-side bushing is required to withstand high voltage and large current from the converter system while simultaneously being subjected to complex electromagnetic and thermal stresses. As a result, the main insulation of the bushing operates over long periods under the coupled effects of superimposed AC-DC electric fields and temperature fields [3–5]. With the successive commissioning of multiple cross-regional UHVDC projects and the continuous construction of new HVDC schemes, the operational reliability of converter equipment, represented by valve-side bushings, has become increasingly important for the security and stability of power grids [6–8].

Currently, dry-type valve-side bushings are widely used in newly built DC projects. Their insulation cores are typically manufactured by winding epoxy-impregnated paper together with metal foils to form a composite insulation structure in combination with SF_6 gas. During long-term operation, partial discharges occurring at the grading electrode layers may lead to the gradual degradation of insulation properties. This degradation process can be further accelerated by thermal effects, forming a detrimental feedback loop that may eventually threaten the normal operation of the bushing and compromise the system safety [9, 10]. Therefore, an in-depth investigation of the insulation behavior of grading electrodes in the main insulation of converter transformer valve-side bushings under coupled electric and thermal fields, together with the establishment of a structural optimization model that simultaneously considers both AC and DC electric field stresses, is of great importance for modern HVDC engineering.

While extensive optimization studies have focused on either AC or DC electric field conditions separately, few studies have integrated both AC and DC stresses in a unified optimization framework. This gap leads to non-optimal insulation margin distributions, limiting the operational reliability of valve-side bushings under real-world combined electric field stresses. Zhu et al. reported that the insulation margin distribution of grading electrodes is nonuniform under AC operating conditions and accordingly proposed an equal-margin iterative design method, which was further validated experimentally [11]. From a thermo-electric coupling perspective, Hammer et al. systematically investigated the influence of internal temperature gradients on the DC electric field distribution within bushings, emphasizing that the overall structural configuration should be comprehensively considered in DC bushing design [12]. With the continuous increase in the voltage levels and internal operating temperatures of valve-side bushings, insulation structures are required to satisfy increasingly stringent performance requirements, motivating researchers to explore more intelligent and systematic design approaches. Hesamzadeh et al. employed an improved genetic algorithm to optimize the grading of electrode parameters under complex constraints, achieving a more balanced distribution of the electric field stress and voltage [13]. Cao et al. proposed an insulation core design method targeting lifetime equalization based on life models derived from accelerated aging tests, while simultaneously considering temperature effects and AC

* Corresponding author: Yongchao Li (1747402356@qq.com).

electric field strength limits [14]. Zhang et al. combined an electro-thermal coupled analysis with particle swarm optimization based on an equal-margin mathematical model, resulting in a more balanced distribution of partial discharge margins and effective control of hotspot temperatures [15].

Overall, most existing studies have focused on structural optimization under either AC or DC electric field conditions alone. The unified optimization of insulation performance under both AC and DC operating conditions, from the perspective of the multi-physical-field coupled environment encountered by converter transformer valve-side bushings, has not yet been sufficiently addressed and still requires further investigation.

To address this gap, this study proposes a multiobjective optimization model that simultaneously considers DC and AC electric field stresses for valve-side bushing insulation structures. Using a 226 kV converter transformer valve-side bushing as the case study, we aim to minimize the variance in insulation margin distributions under combined AC-DC stresses. Based on a comprehensive analysis of the insulation withstand characteristics of its main insulation structure under coupled AC-DC electric fields and temperature fields, a multiobjective optimization model is established that simultaneously considers the uniformity of the DC lifetime margin and AC partial discharge margin. An improved multiobjective grey wolf optimizer (GWO) is then introduced to perform optimization searches on the geometric parameters of grading electrodes, with the aim of improving the utilization efficiency of insulation materials and eliminating potential weak points within the main insulation.

The main contributions of this study are: (1) the development of a unified electro-thermal coupled model for valve-side bushings under AC-DC conditions, (2) the formulation of a multiobjective optimization model to optimize insulation grading structures, and (3) the introduction of an improved GWO to efficiently solve the optimization problem. These contributions provide a new approach to the design and optimization of valve-side bushings in HVDC systems.

2. VALVE SIDE BUSHING STRUCTURE AND MULTI-OBJECTIVE OPTIMIZATION UNDER COMBINED AC-DC ELECTRIC FIELD

2.1. Main Structure of the Valve-Side Bushing

Valve-side bushings in converter transformers adopt a capacitive grading insulation structure composed of multiple metallic foils embedded in epoxy-impregnated paper insulation. The grading electrodes are arranged along the radial direction to control the electric field distribution inside the insulation core and to ensure proper voltage distribution under high-voltage operating conditions. For the convenience of subsequent modeling and theoretical derivations, a brief description of the main insulation structure of the converter transformer valve-side bushing and the correspondence between its key geometric parameters are provided herein. Fig. 1 illustrates a schematic of the valve-side bushing, in which the principal structural parameters are indicated.

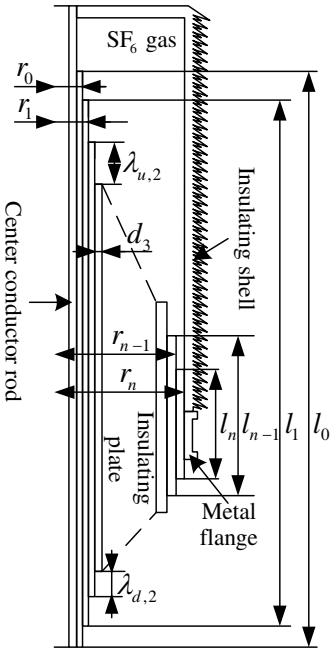

FIGURE 1. Schematic diagram of the main structure of the valve side bushing of the converter transformer.

According to [16–18], the grading structure formed by epoxy-impregnated paper and metal foils inside the valve-side bushing withstands most of the electric-field stress under combined AC-DC voltages. The epoxy-impregnated paper between two adjacent metal foils is treated as one insulation grading layer. The inner-most and outer-most layers are defined as the 0th and nth layers, respectively, and the remaining layers are numbered sequentially. The thickness of the i-th grading layer is defined as

$$d_i = r_i - r_{i-1} \tag{1}$$

For the i-th grading electrode layer ($i \neq n$), the upper- and lower-step lengths between this layer and its adjacent outer layer are denoted as $\lambda_{u,i}$ and $\lambda_{l,i}$, respectively, and satisfy

$$\lambda_{u,i} = k_\lambda \lambda_{l,i} \tag{2}$$

The total step length was equal to the difference between the length of this grading electrode layer and that of its adjacent outer grading electrode layer,

$$\lambda_i = \lambda_{u,i} + \lambda_{l,i} = l_i - l_{i+1} \tag{3}$$

In the optimization process, the dimensions of the central conductor and external insulation are fixed, while the length, thickness, and radial position of the grading electrode layers are treated as the main design variables.

2.2. AC-DC Voltage Operating Conditions and Insulation Design Requirements

In HVDC converter systems, valve-side bushings operate under composite AC-DC voltage stresses. Taking the 226 kV valve-side bushing as an example, the conductor potential under normal operating conditions can be regarded as the superposition of a constant DC component and a power-frequency AC com-

TABLE 1. Technical parameters of 226 kV valve side bushing.

Item	Insulation withstand voltage	Maximum designed withstand field strength
Rated voltage	226 kV	8 kV/mm
Maximum continuous operating voltage	260 kV	8.16 kV/mm
1h dry withstand voltage at power frequency	460 kV	4.5 kV/mm
2h DC withstand voltage	460 kV	12.24 kV/mm

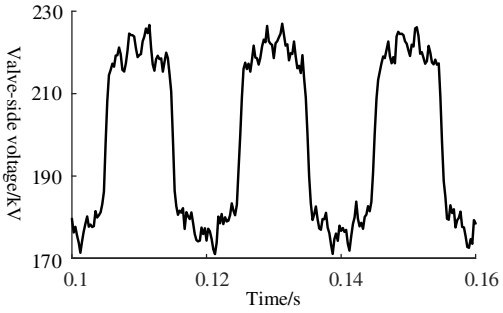

FIGURE 2. Working voltage waveform of valve side bushing of converter transformer.

ponent, as shown in Fig. 2. In addition to the continuous operating voltage, the bushing is also required to withstand various test and transient voltages. The corresponding typical operating and withstand parameters are listed in Table 1.

This mixed-voltage characteristic leads to distinct electric-field distribution mechanisms under DC and AC operating conditions. Under DC conditions, the electric field distribution is mainly governed by the conductivity of the dielectric materials and its temperature dependence, and therefore exhibits a time-dependent redistribution during operation. Under AC conditions, the voltage distribution is mainly determined by the permittivity of each dielectric layer and the geometric configuration of the insulation structure, and is only weakly influenced by temperature.

Accordingly, the insulation design of the valve-side bushing should simultaneously satisfy three requirements:

1) Adequate long-term withstand capability under DC electric stress;

2) Sufficient AC insulation performance to avoid partial discharge or local breakdown;

3) Coordinated insulation-margin distribution among the grading layers to improve material utilization and avoid local weak points.

Therefore, as indicated by the operating conditions in Fig. 2 and the design constraints summarized in Table 1, the valve-side bushing should be optimized under both AC and DC operating conditions. To achieve this, an electro-thermal coupled model and a corresponding multiobjective optimization framework are established in this study.

2.3. Electro-Thermal Coupled Model of the Valve-Side Bushing

Given that the main insulation of a valve-side bushing operates over long periods under the coupled effects of electric and temperature fields and that temperature gradients have a pronounced influence on the DC electric field distribution, an electro-thermal coupled analysis is adopted in this study to model the 226 kV valve-side bushing. A two-dimensional axisymmetric geometry was employed to balance the computational accuracy and cost. The model mainly consists of a central conductor, epoxy-impregnated paper-metal foil grading electrode layers, SF_6 gas, transformer oil, and composite insulator housing, as shown in Fig. 3. For each material region, the corresponding physical properties, including permittivity, thermal conductivity, density, and specific heat capacity, were assigned accordingly.

FIGURE 3. Simulation model of the valve-side bushing.

In the thermal field analysis, the Joule heat generated by the current flowing through the central conductor is considered the dominant volumetric heat source, while the additional losses caused by the dielectric loss and DC leakage current are relatively small and therefore neglected. Accordingly, the volumetric heat source Q satisfies

$$Q = \frac{P_0}{V} = \frac{I_A^2 \cdot \beta \cdot \lambda[1 + \alpha(T - 273.15)] \cdot L/S}{V} \quad (4)$$

where P_0 is the Joule heating power (W); V is the conductor volume (m^3); I_A is the root-mean-square (RMS) current (A); β is the skin effect correction factor; λ is the electrical resistivity of the conductor ($\Omega \cdot m$); α is the temperature coefficient of resistivity (1/K); T is the conductor temperature (K); L is the conductor length (m); and S is the conductor cross-sectional area (m^2).

For the temperature field, heat conduction and convective heat transfer are considered the dominant heat transfer mechanisms, while radiative effects are equivalently included through modified convective heat transfer coefficients. The corresponding thermal boundary conditions are shown in Fig. 4, and the heat transfer coefficients of different interfaces are listed in Table 2. The connection region between the central conductor and the external busbar is approximated as an adiabatic boundary.

TABLE 2. Setting of heat transfer coefficient at bushing interface.

Surface	Heat transfer coefficient/W/m²
Resin-air surface	1
Aluminum-air surface	25
AIP-oil surface	100
Copper-oil surface	120

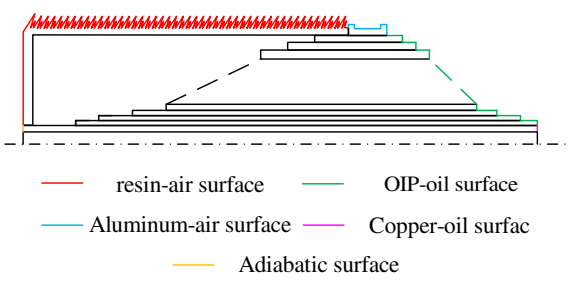

FIGURE 4. Setting of temperature field boundary conditions of valve side bushing.

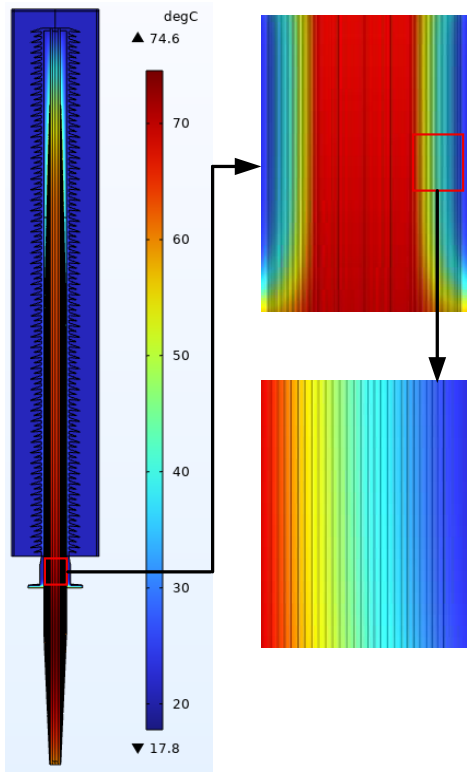

FIGURE 5. Electro–thermal coupled temperature distribution of the valve-side bushing.

The electro-thermal coupled finite-element model was implemented in COMSOL Multiphysics. The calculated temperature distribution is shown in Fig. 5. It can be seen that the temperature inside the valve-side bushing generally decreases from the inner region to the outer region. The temperature ranges from approximately 17.8°C to 74.6°C, with the high-temperature region mainly concentrated around the central conductor because of Joule heating. Along the radial direction, the temperature exhibits an evident gradient, whereas the axial variation is relatively small.

Under DC operating conditions, the electric field distribution in the main insulation is described by the steady-state current continuity equation,

$$\begin{cases} J = \gamma E_{DC} \\ \nabla \cdot E_{DC} = -\nabla \varphi_{DC} \end{cases} \tag{5}$$

where J is the current density (A/m^2); γ is the electrical conductivity of the material (S/m); E_{DC} is the DC electric field strength (V/m); and φ_{DC} is the DC electric potential.

The boundary conditions for the DC electric field are specified as follows: the rated high-potential DC voltage is applied to the central conductor, while the metal flange and outermost aluminum foil electrically connected to it are grounded. All the internal aluminum foils within the insulation core were assigned floating potentials. An infinite element domain is introduced at the outer boundary of the computational model and grounded to simulate the surrounding open space.

Under AC operating conditions, the voltage distribution among the grading electrode layers is calculated using the equivalent capacitor network shown in Fig. 6 [19].

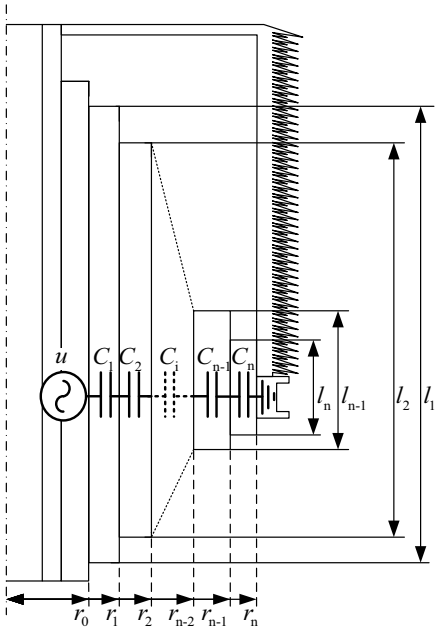

FIGURE 6. Equivalent circuit under AC voltage.

The $n+1$ aluminum foils and n insulation layers form a series-connected equivalent capacitor network. The capacitance of the i-th capacitor, denoted as C_i, satisfies:

$$C_i = \varepsilon_r \varepsilon_0 \frac{l_i}{\ln\left(r_i / r_{i-1}\right)} \tag{6}$$

where ε_r is the relative permittivity of the material, and ε_0 is the vacuum permittivity. Accordingly, the admittance of capacitor C_i at angular frequency ω can be expressed as

$$|B_i| = \frac{1}{\omega C_i} = \frac{\ln\left(r_i / r_{i-1}\right)}{\omega \varepsilon_r \varepsilon_0 l_i} \tag{7}$$

Based on the voltage division relationship of series-connected admittances, the voltage across the i-th capacitor can be expressed as

$$U_i = \frac{|B_i|}{\sum_{k=1}^{n} |B_k|} U \tag{8}$$

and the corresponding electric field strength is expressed as:

$$E_i = \frac{U_i}{d_i} = \frac{U_i}{r_i - r_{i-1}} \tag{9}$$

By combining the electro-thermal model and the AC equivalent circuit, the electric field and temperature distributions of the valve-side bushing under both DC and AC operating conditions can be obtained. These results provide the basis for the subsequent definition of insulation margin indices and the construction of the multiobjective optimization model.

2.4. Multiobjective Optimization Model under Combined AC-DC Electric Field

The multiobjective optimization model of the valve-side bushing is established by defining its objective functions, decision variables, and constraints.

2.4.1. Selection of Objective Function

Because the valve-side bushing operates under both DC and AC electric stresses, its insulation design must simultaneously satisfy long-term DC withstand requirements and AC partial discharge constraints. Therefore, the distributions of insulation margins under the two operating conditions are selected as the optimization targets.

a) Insulation Margin Index under DC Electric Field: Under DC operating conditions, the insulation margin is mainly determined by the long-term withstand electric field strength of the dielectric and its aging state. According to the accelerated aging data reported in [20], the maximum long-term DC withstand electric field varies with temperature. Based on the fitting method in [14], the relationship between temperature and long-term electric field strength can be expressed as

$$E_M(T) = k_E e^{-k_T T} \tag{10}$$

where T is the temperature experienced by the insulation medium; $E_M(T)$ denotes the maximum long-term DC withstand electric field strength of the insulation at temperature T; and k_E and k_T are fitting constants obtained from the experimental data, which are related to the intrinsic properties of the insulation material.

By substituting the above expression, the DC insulation margin of the insulation medium at temperature T under the DC electric field strength E_{DC}, denoted as $Mar_{DC}(T)$, can be expressed as:

$$Mar_{DC}(T) = \frac{E_M(T)}{E_{DC}} = \frac{k_E e^{-k_T T}}{E_{DC}} \tag{11}$$

b) Insulation Margin Index under an AC Electric Field: Under AC operating conditions, the insulation margin is mainly related to the partial discharge inception characteristics of the grading structure. As reported in [15], the partial discharge inception voltage $U_{PD}(d)$ is positively correlated correlation with the electrode thickness d, and can be written as

$$U_{PD}(d) = k_{PD} \left(\frac{d}{\varepsilon_r} \right)^{0.45} \tag{12}$$

where k_{PD} is an empirical coefficient obtained from the experimental results, and ε_r is the relative permittivity of the insulation material.

Since the grading electrode layers can be approximated as slender cylindrical capacitors, the corresponding partial-discharge inception electric field can be expressed as:

$$E_{PD}(d) = \frac{U_{PD}}{d} = k_{PD} \frac{d^{-0.55}}{\varepsilon_r^{0.45}} \tag{13}$$

Thus, the AC insulation margin under an AC electric field E_{AC} is defined as:

$$Mar_{AC}(d) = \frac{E_{PD}(d)}{E_{AC}} = \frac{k_{PD} d^{-0.55}}{\varepsilon_r^{0.45} E_{AC}} \tag{14}$$

c) Normalized Variance Objective Functions and Multiobjective Optimization Model: To maximize insulation utilization and avoid local weak points, the uniformity of the insulation margin distribution among grading layers is taken as the optimization objective. Therefore, the normalized variances of the DC and AC insulation margins are adopted as the two objective functions:

$$\begin{cases} f_1 = \min \frac{Var_{DC}}{\overline{Mar}_{DC}} = \min \frac{\sum_{i=1}^{n} (Mar_{DC,i} - \overline{Mar}_{DC})}{(n-1)\overline{Mar}_{DC}} \\ f_2 = \min \frac{Var_{AC}}{\overline{Mar}_{AC}} = \min \frac{\sum_{i=1}^{n} (Mar_{AC,i} - \overline{Mar}_{AC})}{(n-1)\overline{Mar}_{AC}} \end{cases} \tag{15}$$

where $Mar_{DC,i}$ and $Mar_{AC,i}$ denote the insulation margins of the i-th insulation grading electrode layer under DC and AC electric field conditions, respectively, which are given by:

$$\begin{cases} Mar_{DC,i} = \frac{k_E e^{-k_T \overline{T}_i}}{E_{DC,i}^{\max}} \\ Mar_{AC,i} = \frac{k_{PD} d_i^{-0.55}}{\varepsilon_r^{0.45} E_{AC,i}^{\max}} \end{cases} \tag{16}$$

where $\overline{T_i}$ is the average spatial temperature of the i-th insulation grading electrode layer. The average temperature is used to evaluate the insulation withstand capability based on the average withstand electric field within the layer, thereby reducing the complexity of the degradation model. $E_{DC,i}^{\max}$ denotes the maximum DC electric field strength within the i-th insulation grading electrode layer, and d_i is the thickness of the i-th layer. $E_{AC,i}^{\max}$ represents the maximum AC electric field strength within the i-th insulation grading electrode layer. The maximum values of the DC and AC electric field strengths were

adopted to assess the main insulation of the valve-side bushing under the most severe insulation stress conditions to ensure sufficient operational reliability. Furthermore, $\overline{Mar}_{DC}$ and $\overline{Mar}_{AC}$ denote the average insulation margins of the grading electrode layers under the DC and AC electric field conditions, respectively.

$$\begin{cases} \overline{Mar}_{DC} = \dfrac{\sum_{i=1}^{n} Mar_{DC,i}}{n} \\ \overline{Mar}_{AC} = \dfrac{\sum_{i=1}^{n} Mar_{AC,i}}{n} \end{cases} \tag{17}$$

Because the DC electric field is mainly governed by conductivity, whereas the AC electric field is mainly determined by permittivity and geometry, the two objectives are inherently conflicting. Therefore, the insulation design of the valve-side bushing is formulated as a multiobjective optimization problem.

2.4.2. Selection of Decision Variables

As discussed above, the insulation margins under both AC and DC operating conditions are strongly dependent on the geometric parameters of the grading electrode layers. Therefore, the optimization variables should be selected from the axial and radial dimensions of the grading structure.

To reduce the complexity of the optimization problem while preserving the main design flexibility, the inner diameter and axial length of the innermost grading electrode, as well as the outer diameter and axial length of the outermost grading electrode, are fixed according to the equal-capacitance reference design under AC operating conditions. On this basis, the step-length sequence of the intermediate grading electrodes and the thickness correction terms of each grading layer are selected as the decision variables.

With this treatment, the variable ranges are confined to reasonable intervals, and the monotonic geometric relationship of the grading structure can be naturally maintained. As a result, the overall complexity of the optimization model is effectively reduced.

2.4.3. Integration of Constraint Conditions

In the insulation structure optimization model, constraint conditions are formulated to impose limitations and characterize the geometric configuration, fundamental insulation design requirements, and electric field distributions under both AC and DC operating conditions.

First, for the i-th step length and thickness correction of the grading electrode layer, which are taken as decision variables, the correction terms $\Delta_{\lambda,i}$ and $\Delta_{d,i}$ are constrained by their corresponding lower and upper bounds, respectively, that is,

$$\begin{aligned} \Delta_{\lambda,\min} < \Delta_{\lambda,i} < \Delta_{\lambda,\max}, \quad 1 < i < n-1 \\ \Delta_{d,\min} < \Delta_{d,i} < \Delta_{d,\max}, \quad 1 < i < n-1 \end{aligned} \tag{18}$$

where $\Delta_{\lambda,\min}$ and $\Delta_{\lambda,\max}$ denote the lower and upper bounds of the correction term for the step length, respectively, and $\Delta_{d,\min}$ and $\Delta_{d,\max}$ represent the lower and upper bounds of the correction term for the graded electrode thickness, respectively.

Accordingly, based on the original step length λ_i and grading electrode thickness d_i, the corrected step length λ_i' and corrected thickness d_i' of the i-th grading electrode layer can be obtained as follows:

$$\begin{aligned} \lambda_i' &= \lambda_i + \Delta_{\lambda,i}, \quad 2 < i < n-1 \\ d_i' &= d_i + \Delta_{d,i}, \quad 2 < i < n-1 \end{aligned} \tag{19}$$

The corrected parameters are also required to satisfy the corresponding lower and upper bounds, as follows:

$$\begin{aligned} \lambda^{\min} \le \lambda_i' \le \lambda^{\max} \\ d^{\min} \le d_i' \le d^{\max} \end{aligned} \tag{20}$$

where $\lambda^{\min}$ and $\lambda^{\max}$ denote the lower and upper bounds of the step length, respectively, and $d^{\min}$ and $d^{\max}$ denote the lower and upper bounds of the grading electrode thickness, respectively.

Finally, based on the length l_{i-1} and radius r_{i-1} of the $(i-1)$th grading electrode layer, the corrected length l_i' and radius r_i' of the i-th grading electrode layer can be obtained, as follows:

$$\begin{aligned} l_i' &= l_{i-1} - \lambda_i', \quad 2 < i < n-1 \\ r_i' &= r_{i-1} + d_i', \quad 2 < i < n-1 \end{aligned} \tag{21}$$

By using the above formulation, the geometric monotonicity of the grading electrode structure can be naturally preserved, and a complete set of geometric constraints is established for the subsequent optimization process.

3. IMPROVED MULTIOBJECTIVE GWO FOR INSULATION OPTIMIZATION

3.1. Standard Multiobjective GWO

The standard multiobjective grey wolf optimizer (MOGWO) is adopted in this study to solve the proposed insulation optimization problem. Owing to its hierarchical population structure and external archive mechanism, MOGWO is suitable for handling multiobjective optimization problems [21–23].

However, when applied to complex engineering optimization problems, the standard MOGWO still exhibits two limitations. First, the linear convergence factor may lead to a premature reduction of global exploration ability. Second, the diversity maintenance of the external archive is only activated when the archive becomes full, which makes it difficult to continuously regulate the distribution uniformity of nondominated solutions. These shortcomings may reduce the final quality of the Pareto solution set.

To address these issues, an improved nonlinear convergence factor and a crowding-solution screening-elimination mechanism are introduced in this study [24–26].

3.2. Improved Nonlinear Convergence Factor

In the standard GWO, the convergence factor decreases linearly with the number of iterations:

$$a(t) = a_{\max} - (a_{\max} - a_{\min})\frac{t}{t_{\max}} \tag{22}$$

where $a_{\max}$ and $a_{\min}$ are the maximum and minimum convergence factors; t is the current iteration number; and $t_{\max}$ is the maximum number of iterations.

To improve the balance between global exploration and local exploitation, a cosine-based nonlinear convergence factor is adopted:

$$a = \frac{a_{\max} - a_{\min}}{2}\left[\cos\left(\frac{\pi t}{t_{\max}}\right) + 1\right] \tag{23}$$

In this study, $a_{\max} = 2$ and $a_{\min} = 0$. As shown in Fig. 7, the proposed formulation slows down the decay of the convergence factor in the early stage and accelerates it in the later stage. This improves the balance between global exploration and local exploitation, thereby alleviating premature convergence and improving the Pareto solution quality.

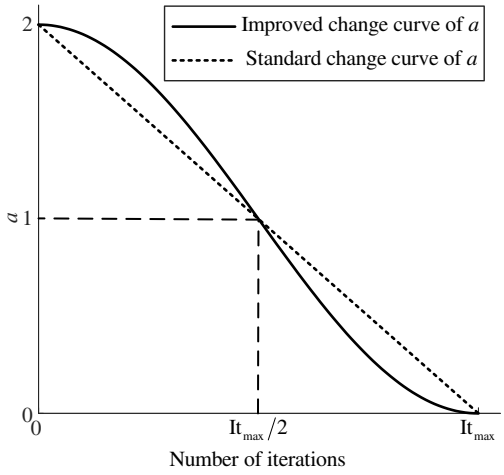

FIGURE 7. Change curve of iteration factor a before and after improvement.

3.3. Crowding Solution Screening-Elimination Mechanism

In multiobjective optimization, the nondominated solutions stored in the external archive may become unevenly distributed. In the standard algorithm, archive regulation is performed only when the archive becomes full, which is insufficient for continuously improving the diversity of the solution set during the evolutionary process.

To improve the distribution quality of the archive, a crowding-solution screening-elimination mechanism based on the average minimum distance is introduced. Whenever a new nondominated solution is added, and the number of archived solutions exceeds a preset threshold, the crowded-solution screening procedure is activated.

For the i-th solution f_i in the archive, the minimum distance $d_{\min,i}$ is defined as:

$$d_{\min,i} = \begin{cases} d(f_1, f_2) & i = 1 \\ \min\left[d(f_{i-1}, f_i), d(f_i, f_{i+1})\right] & i = 2, \ldots, n-1 \\ d(f_{n-1}, f_n) & i = n \end{cases} \tag{24}$$

where $d(f_a, f_b)$ denote the Euclidean distance between the a-th and b-th solutions in the objective space. The corresponding average minimum distance is

$$\overline{d_{\min}} = \frac{\sum_{i=1}^{n} d_{\min,i}}{n} \tag{25}$$

If the i-th solution satisfies $d_{\min,i} < k_d\overline{d_{\min}}$, it is identified as a crowded solution, where k_d is a prescribed proportional coefficient. All identified crowded solutions are then removed from the external archive.

By performing this operation throughout the optimization process, the nondominated solutions can be kept more uniformly distributed, and low-quality crowded solutions can be prevented from occupying the archive for long periods. Consequently, the diversity and representativeness of the final Pareto solution set are improved.

In the optimization design of the main insulation of the valve-side bushing, the axial lengths and radial parameters of each grading electrode layer were represented using real-coded encoding. On this basis, the original linear convergence factor was replaced by the proposed nonlinear convergence factor, and the crowded-solution screening and elimination module was incorporated, thereby forming the improved multiobjective GWO adopted in this study. The overall implementation procedure of the proposed algorithm is summarized in Fig. 8.

3.4. Benchmark Validation of the Proposed Algorithm

To further verify the general applicability of the proposed algorithm beyond the engineering case study, several standard multiobjective benchmark functions were employed. In this study, the classical test functions ZDT1, ZDT2, ZDT3, and DTLZ2 were selected because they represent different Pareto-front characteristics, including convex, non-convex, discontinuous, and high-dimensional Pareto sets.

The performance of the proposed algorithm was compared with two widely used multiobjective optimization algorithms, namely NSGA-II and the standard multiobjective GWO (MOGWO). For a fair comparison, the population size and maximum number of iterations were set to 100 and 200, respectively, for all algorithms.

Two widely used performance metrics were adopted to evaluate the quality of the obtained Pareto solution sets:

Hypervolume (HV), which reflects both convergence and diversity of the Pareto front.

Inverted Generational Distance (IGD), which measures the distance between the obtained Pareto front and the true Pareto front.

Each algorithm was independently run 20 times, and the average high voltage (HV) and IGD values were recorded. Table 3 summarizes the optimization results of the three algorithms on the benchmark problems.

TABLE 3. Performance comparison of different algorithms on benchmark test functions.

Test functio	Algorithm	HV	IGD
ZDT1	NSGA-II	0.713	0.0118
	MOGWO	0.741	0.0097
	Proposed	0.768	0.0079
ZDT2	NSGA-II	0.684	0.0146
	MOGWO	0.721	0.0115
	Proposed	0.752	0.0088
ZDT3	NSGA-II	0.647	0.0173
	MOGWO	0.689	0.0138
	Proposed	0.724	0.0106
DTLZ2	NSGA-II	0.618	0.0194
	MOGWO	0.663	0.0151
	Proposed	0.701	0.0117

The results show that the proposed algorithm consistently achieves higher HV values and lower IGD values, indicating better convergence performance and improved diversity of the obtained Pareto solution set. Therefore, the benchmark tests further confirm the effectiveness and robustness of the proposed optimization strategy.

4. ENGINEERING VALIDATION OF THE PROPOSED ALGORITHM

To verify the effectiveness of the proposed algorithm in a practical engineering problem, a 226 kV converter transformer valve-side bushing with a rated current of 3 kA was selected as the case study. Multiobjective optimization was carried out using both the standard MOGWO and the proposed improved algorithm, and the obtained Pareto solution sets were compared using relevant performance indicators.

In this case study, the insulation core consisted of 27 grading electrode layers, and the initial structure was obtained from the equal-capacitance reference design. The correction range of the axial step length was set to $[-100, 100]$ mm, and the thickness correction range was set to $[-2, 2]$ mm. The population size, archive size, and maximum number of iterations were set to 140, 80, and 500, respectively.

Under DC operating conditions, the steady-state field distribution was evaluated using the rated DC voltage and operating temperature. Under AC operating conditions, the power-frequency component superimposed on the DC voltage was considered according to International Electrotechnical Commission (IEC) requirements. The electro-thermal finite element model was used to calculate the temperature and DC electric field distributions, while the AC equivalent circuit was used to determine the interlayer voltage distribution and corresponding electric field strengths.

The Pareto-optimal solution sets obtained by the standard and improved algorithms are shown in Fig. 9. Both algorithms can identify nondominated solutions; however, the proposed method yields a Pareto set that is closer to the origin and more uniformly distributed. This indicates that the improved convergence strategy and crowding-solution elimination mechanism enhance both convergence quality and solution diversity.

To evaluate the uniformity of the obtained nondominated solution set in the solution space, the deviation index can be adopted as a quantitative metric. Its definition is given by:

$$SP = \sum_{i=1}^{n-1} \frac{|d_i - \bar{d}|}{n-1} \tag{26}$$

A smaller SP value indicates a more uniform distribution of the Pareto solution set.

The diversity of the nondominated solution set can be evaluated using the HV indicator.

Both algorithms were applied to the multiobjective optimization design of the converter transformer valve-side bushing. Each algorithm was independently executed ten times, and the corresponding deviation index and hypervolume indicator were statistically analyzed. The results are summarized in Table 4. It can be observed that the improved algorithm yields a smaller deviation index and a larger hypervolume value, indicating that the resulting Pareto solution set exhibits a more uniform distribution in the solution space and significantly enhances solution diversity.

Therefore, the improved algorithm exhibits better convergence and diversity performance in the practical valve-side bushing optimization problem, which provides a more reliable basis for the subsequent design analysis.

5. DISCUSSION

5.1. Analysis of Design Results

After verifying the effectiveness of the proposed optimization algorithm, the design results of the valve-side bushing are further analyzed in this subsection. Using the same converter transformer valve-side bushing as the case study, conventional single-objective equal-margin optimizations were first carried out separately under AC and DC operating conditions. The normalized variances of the insulation margins under both electric field conditions were then calculated for the two resulting designs, as summarized in Table 5. It can be seen that when the structure is optimized in a single-objective manner for one operating condition, the insulation margin distribution under the other condition deteriorates significantly, exhibiting poorer uniformity and larger interlayer discrepancies.

Table 6 lists a representative set of Pareto solutions obtained using the improved multiobjective GWO. The normalized variances under DC and AC operating conditions are compared with those of the corresponding single-objective equal-margin designs shown in Table 5. The results show that, for an individual objective, a multiobjective optimized design is generally slightly inferior to the corresponding single-objective optimum. However, from the perspective of the overall trade-off between

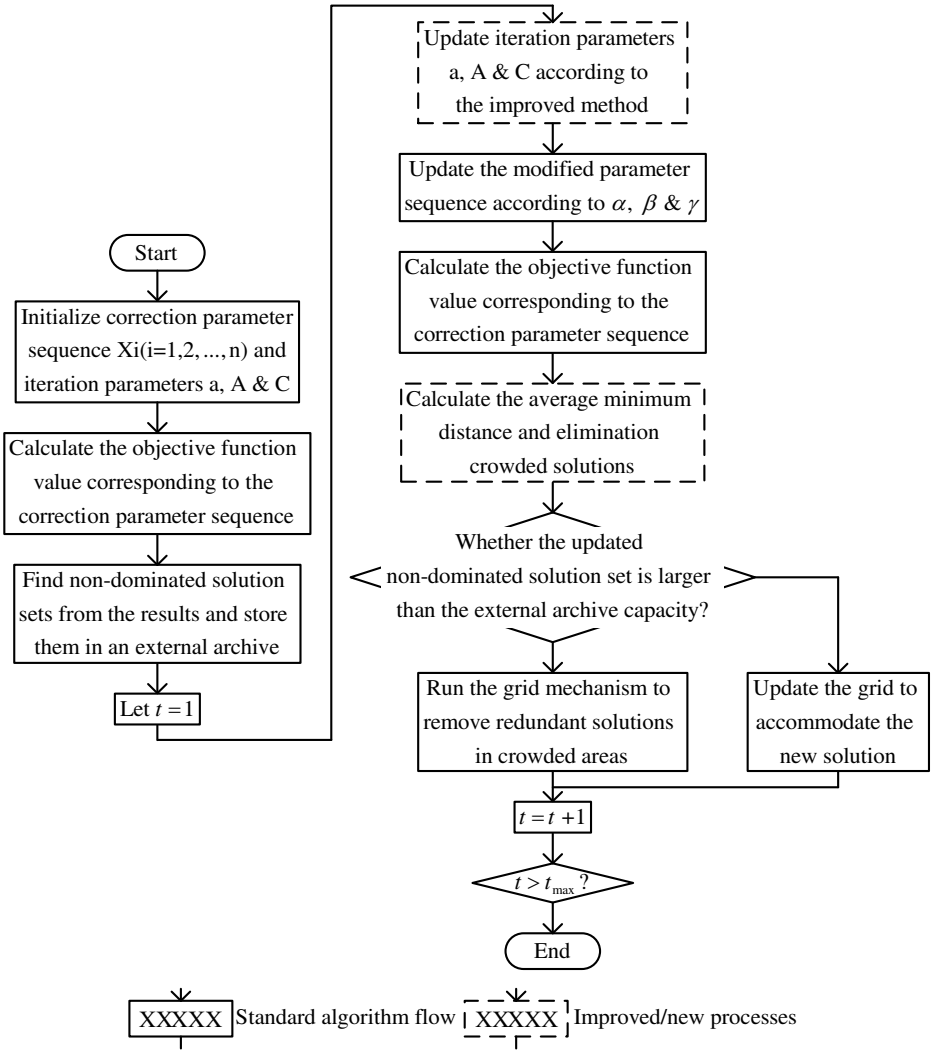

FIGURE 8. Flowchart of the improved multiobjective GWO.

TABLE 4. Comparison of SP and HV values obtained by the standard and improved algorithms.

Number of runs	$DI/\times10^{-3}$		$HV/\times10^{-3}$	
	Standard algorithms	Improved algorithms	Standard algorithms	Improved algorithms
1	1.020	0.646	5.897	8.782
2	1.076	0.614	5.104	8.935
3	1.064	0.643	5.479	9.416
4	0.968	0.694	5.722	9.262
5	1.024	0.745	6.284	8.843
6	1.119	0.706	5.384	8.967
7	1.007	0.658	5.197	9.035
8	1.016	0.747	4.882	9.368
9	0.986	0.716	5.645	9.117
10	0.918	0.694	6.121	8.873

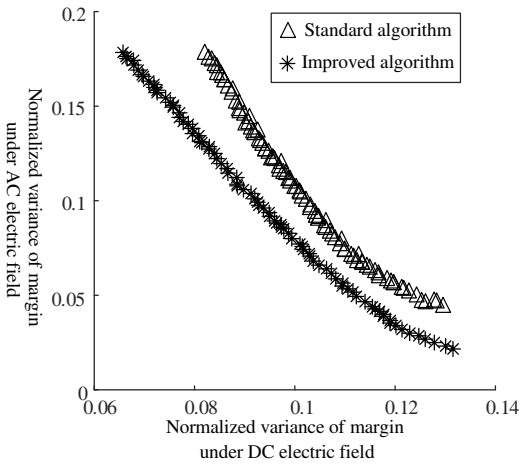

FIGURE 9. Distribution of Pareto optimal solutions obtained by standard and improved algorithms.

the two objectives, the multiobjective solutions exhibit better comprehensive performance. This clearly demonstrates the advantage of the proposed multiobjective optimization method in coordinating the insulation performance of the valve-side bushing under combined AC and DC electric field conditions.

5.2. Electric Field Distribution before and after Optimization

To further verify the effectiveness of the proposed optimization method, the electric field distributions of the valve-side bushing before and after optimization were analyzed under both DC and AC operating conditions. The corresponding electric field distribution cloud maps are shown in Figs. 10 and 11, and the radial electric field distributions extracted from the grading electrode layers at the flange region are presented in Figs. 12 and 13, respectively.

Under DC operating conditions, the electric field is mainly concentrated in the outer grading electrode region. As shown in Fig. 10, the maximum DC electric field decreases from approximately 8.4 kV/mm before optimization to 7.88 kV/mm after optimization, corresponding to a reduction of about 6.2%. At the flange region, the extracted radial electric field in Fig. 12 shows that the peak value decreases from about 5.2 kV/mm to 4.8 kV/mm, while the fluctuation amplitude among adjacent grading layers is reduced. These results indicate that the DC electric stress is redistributed more uniformly after optimization.

Under AC operating conditions, a similar improvement can be observed. As shown in Fig. 11, the maximum AC electric field decreases from approximately 1.64 kV/mm to 1.47 kV/mm, corresponding to a reduction of about 10.4%. The radial electric field distribution at the flange region in Fig. 13 further shows that the field variation becomes less pronounced after optimization, with the peak value decreasing from about 1.0 kV/mm to 0.95 kV/mm. This redistribution is mainly attributed to the coordinated adjustment of the grading electrode geometry, which moderates the electric field gradient between adjacent layers.

Overall, the optimized grading electrode structure effectively reduces the peak electric field strength and improves the uniformity of the electric field distribution under both DC and AC operating conditions. This is consistent with the optimization objective of minimizing the normalized variance of insulation margins and demonstrates that the proposed method can alleviate local electric field concentration and enhance insulation coordination in the valve-side bushing.

TABLE 5. Summary of single-objective optimization results.

Optimization goal	Normalized variance of margin	
	DC electric field	AC electric field
Margin under DC electric field	0.042	0.250
Margin under AC electric field	0.155	1.954×10^{-6}

5.3. Engineering Implications

From an engineering perspective, the optimized grading electrode structure provides clear practical benefits for the insulation design of valve-side bushings operating under composite AC-DC electric stresses. According to the simulation results, the maximum DC electric field decreases from 8.4 kV/mm to 7.88 kV/mm, corresponding to a reduction of about 6.2%, while the maximum AC electric field decreases from 1.64 kV/mm to 1.47 kV/mm, corresponding to a reduction of about 10.4%. In addition, the peak radial electric field at the flange region decreases from approximately 5.2 kV/mm to 4.8 kV/mm under DC conditions and from 1.0 kV/mm to 0.95 kV/mm under AC conditions. These results indicate that the optimized structure effectively suppresses local electric-field concentration and helps mitigate insulation overstressing.

The optimization also improves the uniformity of the electric field distribution among the grading electrode layers. The reduced fluctuation amplitude of the radial electric field indicates a more balanced electric-stress distribution after optimization. Correspondingly, the insulation margin distribution among different grading layers becomes more coordinated, which is consistent with the reduction in the normalized variance of insulation margins. This means that the optimized structure not only lowers the peak electric field, but also improves the utilization efficiency of the insulation structure by avoiding local weak points and excessive design redundancy.

These improvements are beneficial for the long-term reliability and practical engineering design of valve-side bushings. Since the DC electric field is closely related to long-term electrical aging and the AC electric field is associated with partial discharge inception, reducing the peak field by approximately 6–10% and improving the electric-field uniformity can effectively lower the risk of local insulation degradation. Therefore, the proposed multiobjective optimization strategy provides a practical design approach for enhancing insulation reliability, improving insulation coordination, and increasing material utilization efficiency in HVDC equipment.

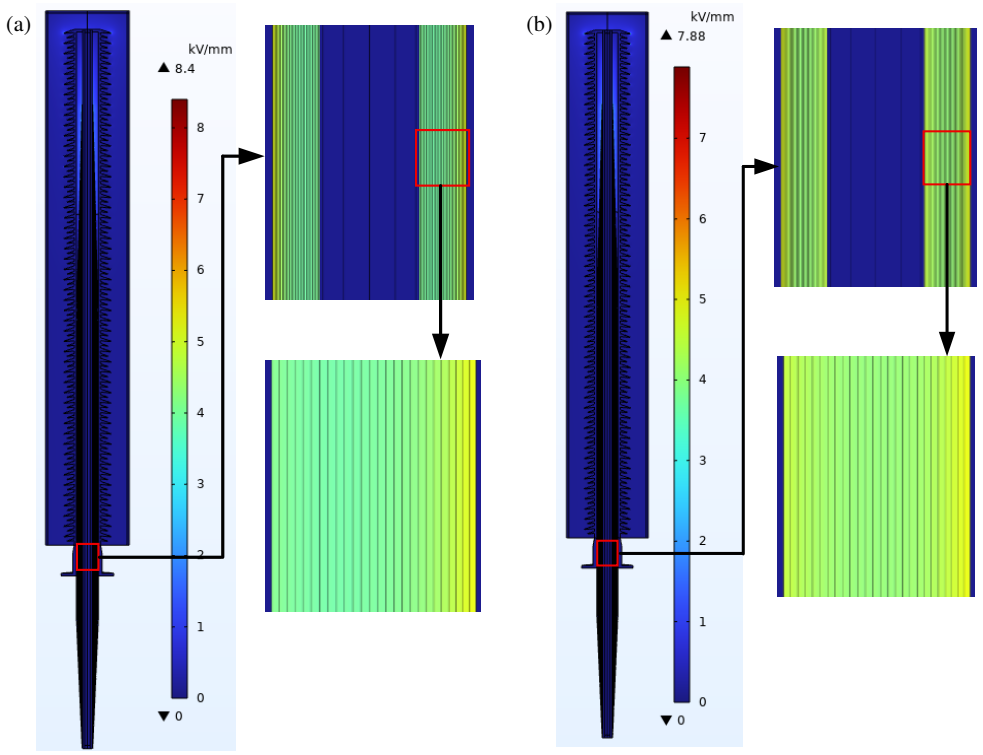

Before optimization After optimization

FIGURE 10. DC electric field distribution before and after optimization.

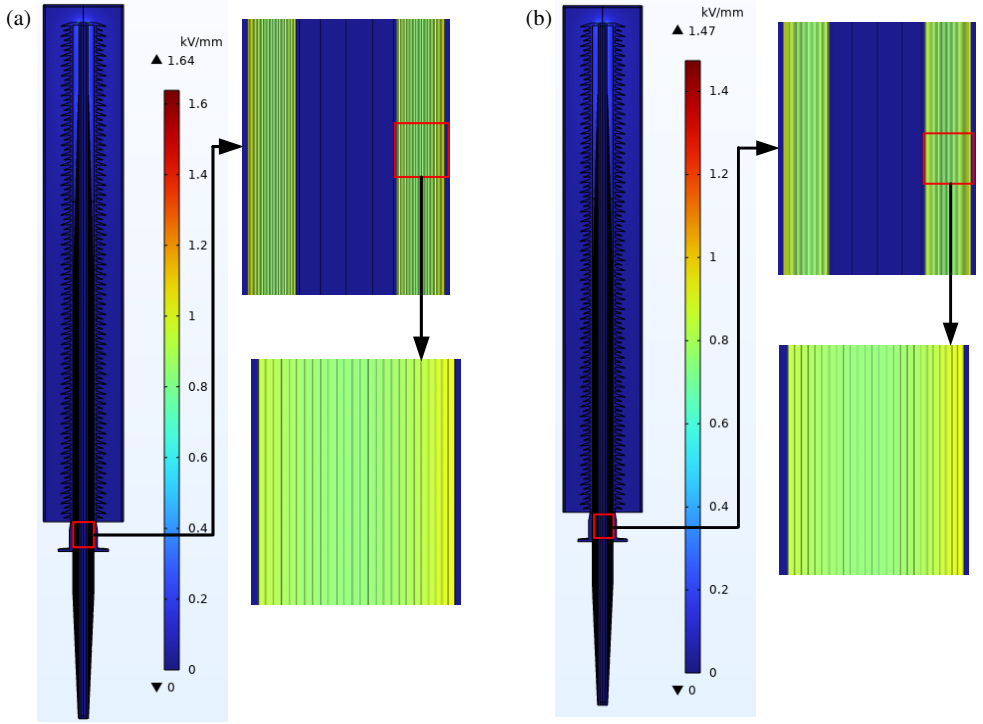

Before optimization After optimization

FIGURE 11. AC electric field distributions before and after optimization.

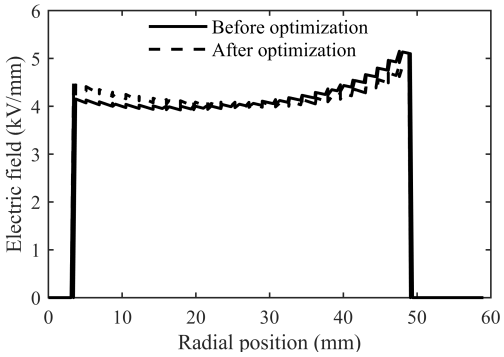

FIGURE 12. Radial DC electric field distribution before and after optimization.

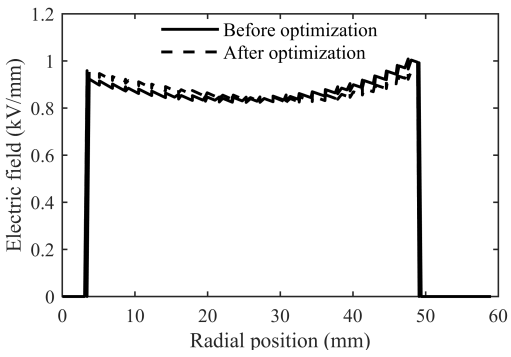

FIGURE 13. Radial AC electric field distribution before and after optimization.

TABLE 6. Statistics of insulation margin variance obtained by the improved multiobjective optimization.

Serial number	Normalized variance of margin			
	DC electric field		AC electric field	
	Value	The effect of optimization/%	Value	The effect of optimization/%
1	0.071	−55.07	0.180	−27.80
2	0.078	−50.86	0.157	−36.82
3	0.082	−47.03	0.141	−44.17
4	0.087	−43.88	0.124	−50.86
5	0.094	−39.22	0.108	−56.25
6	0.095	−38.43	0.102	−58.71
7	0.103	−35.29	0.088	−64.35
8	0.106	−30.54	0.070	−72.49
9	0.124	−21.99	0.047	−80.56
10	0.135	−15.56	0.036	−86.07

6. CONCLUSION

A multiobjective optimization method for the insulation structure of a converter transformer valve-side bushing under combined AC-DC electric stresses was proposed based on an electro-thermal coupled model and an improved multiobjective grey wolf optimizer.

The results show that the proposed method improves both the Pareto-solution quality and the insulation-field distribution. Compared with the standard algorithm, the improved method yields a lower spacing metric (SP) value and a higher HV value, indicating better uniformity and diversity of the obtained Pareto solution set. In addition, the optimized structure reduces the maximum DC electric field from 8.4 kV/mm to 7.88 kV/mm and the maximum AC electric field from 1.64 kV/mm to 1.47 kV/mm, corresponding to reductions of about 6.2% and 10.4%, respectively. The radial electric field at the flange region also becomes more uniform after optimization.

Overall, the proposed method effectively suppresses local electric-field concentration and improves insulation coordination under composite AC-DC operating conditions. Therefore, it provides a practical design approach for enhancing the reliability and material utilization efficiency of valve-side bushings and other capacitive grading insulation structures in HVDC equipment.

ACKNOWLEDGEMENT

This research was supported by the Science and Technology Project of Guangdong Power Grid Co., Ltd., under Grant No. GDKJXM20240406.

REFERENCES

[1] Alassi, A., S. Bañales, O. Ellabban, G. Adam, and C. MacIver, "Hvdc transmission: Technology review, market trends and future outlook," *Renewable and Sustainable Energy Reviews*, Vol. 112, 530–554, Sep. 2019.

[2] Murugan, R. and R. Ramasamy, "Understanding the power transformer component failures for health index-based maintenance planning in electric utilities," *Engineering Failure Analysis*, Vol. 96, 274–288, Feb. 2019.

[3] Chen, M., X. Liu, Y. Shao, H. Tang, Z. Wu, Q. Zhang, and J. Li, "Cracking risk analysis and control for high-voltage dry-type valve-side bushings," *IET Generation, Transmission & Distribution*, Vol. 14, No. 26, 6555–6561, Dec. 2020.

[4] Yang, L., Z. Cheng, L. Cheng, and R. Liao, "Influence of oil-paper configuration on electric field distribution of main insulation structure on valve-side winding of UHV-DC converter transformer," *IET Science, Measurement & Technology*, Vol. 16, No. 2, 90–100, Mar. 2022.

[5] Du, B., R. Chang, W. Zhu, J. Li, and J. Jiang, "Temperature-dependent surface charge and discharge behaviour of converter transformer oil-paper insulation under DC voltage," *IET Science, Measurement & Technology*, Vol. 13, No. 1, 29–34, Jan. 2019.

[6] Van Hertem, D., W. Leterme, G. Chaffey, M. Abedrabbo, M. Wang, F. Zerihun, and M. Barnes, "Substations for future HVdc grids: Equipment and configurations for connection of HVdc network elements," *IEEE Power and Energy Magazine*, Vol. 17, No. 4, 56–66, Jul.–Aug. 2019.

[7] Li, B., J. Liu, Z. Wang, S. Zhang, and D. Xu, "Modular high-power DC-DC converter for MVDC renewable energy collection systems," *IEEE Transactions on Industrial Electronics*, Vol. 68, No. 7, 5875–5886, Jul. 2021.

[8] Acevedo, A. L. F., A. Jahanbani-Ardakani, H. Nosair, A. Venkataraman, J. D. McCalley, A. Bloom, D. Osborn, J. Caspary, J. Okullo, J. Bakke, and H. Scribner, "Design and valuation of high-capacity HVDC macrogrid transmission for the continental US," *IEEE Transactions on Power Systems*, Vol. 36, No. 4, 2750–2760, Jul. 2021.

[9] Li, J., X. Han, Z. Liu, X. Yao, and Y. Li, "PD characteristics of oil-pressboard insulation under AC and DC mixed voltage," *IEEE Transactions on Dielectrics and Electrical Insulation*, Vol. 23, No. 1, 444–450, Feb. 2016.

[10] Wei, Y.-H., H.-B. Mu, G.-J. Zhang, and G. Chen, "A study of oil-impregnated paper insulation aged with thermal-electrical stress: PD characteristics and trap parameters," *IEEE Transactions on Dielectrics and Electrical Insulation*, Vol. 23, No. 6, 3411–3420, Dec. 2016.

[11] Zhu, F., J. Ju, and Z. Zhao, "Optimal design of HV transformer bushing," in *IEEE 3rd Int'l. Conf. Properties and Applications of Dielectric Materials*, 434–437, Tokyo, Japan, Jul. 1991.

[12] Hammer, F. and A. Kuchler, "Insulating systems for HVDC power apparatus," *IEEE Transactions on Electrical Insulation*, Vol. 27, No. 3, 601–609, Jun. 1992.

[13] Hesamzadeh, M. R., N. Hosseinzadeh, and P. Wolfs, "An advanced optimal approach for high voltage AC bushing design," *IEEE Transactions on Dielectrics and Electrical Insulation*, Vol. 15, No. 2, 461–466, Apr. 2008.

[14] Cao, W., W. Shen, B. He, and K. Wu, "Structural design for DC bushing core based on the material life," *IEEE Transactions on Dielectrics and Electrical Insulation*, Vol. 20, No. 1, 281–288, Feb. 2013.

[15] Zhang, S., Z. Peng, and P. Liu, "Inner insulation structure optimization of UHV RIP oil-SF6 bushing using electro-thermal simulation and advanced equal margin design method," *IEEE Transactions on Dielectrics and Electrical Insulation*, Vol. 21, No. 4, 1768–1777, Aug. 2014.

[16] Du, B., H. Sun, J. Jiang, X. Kong, and W. Yang, "Temperature-dependent electric field distribution in ±800 kV valve-side bushing insulation for a converter transformer," *High Voltage*, Vol. 6, No. 1, 106–115, Feb. 2021.

[17] Wang, Q., G. Xie, H. Tian, Z. Peng, and X. Yang, "Electro-thermal coupling field simulation of converter transformer valve side bushings," *IEEJ Transactions On Electrical And Electronic Engineering*, Vol. 16, No. 2, 248–258, Feb. 2021.

[18] Akbari, M., M. Allahbakhshi, and R. Mahmoodian, "Heat analysis of the power transformer bushings in the transient and steady states considering the load variations," *Applied Thermal Engineering*, Vol. 121, 999–1010, Jul. 2017.

[19] Tang, H., G. Wu, J. Deng, M. Chen, X. Li, and K. Liu, "Electro-thermal comprehensive analysis method for defective bushings in HVDC converter transformer valve-side under multiple-frequency voltage and current harmonics," *International Journal of Electrical Power & Energy Systems*, Vol. 130, 106777, Sep. 2021.

[20] Yang, L. J., W. Sun, S. Gao, and J. Hao, "Thermal aging test for transformer oil-paper insulation under over-load condition temperature," *IET Generation, Transmission & Distribution*, Vol. 12, No. 12, 2846–2853, Jul. 2018.

[21] Mirjalili, S., S. Saremi, S. M. Mirjalili, and L. D. S. Coelho, "Multi-objective grey wolf optimizer: A novel algorithm for multi-criterion optimization," *Expert Systems with Applications*, Vol. 47, 106–119, Apr. 2016.

[22] Mirjalili, S., S. M. Mirjalili, and A. Lewis, "Grey wolf optimizer," *Advances in Engineering Software*, Vol. 69, 46–61, Mar. 2014.

[23] Makhadmeh, S. N., O. A. Alomari, S. Mirjalili, M. A. Al-Betar, and A. Elnagar, "Recent advances in multi-objective grey wolf optimizer, its versions and applications," *Neural Computing and Applications*, Vol. 34, No. 22, 19 723–19 749, 2022.

[24] Liu, J., Z. Yang, and D. Li, "A multiple search strategies based grey wolf optimizer for solving multi-objective optimization problems," *Expert Systems with Applications*, Vol. 145, 113134, May 2020.

[25] Yang, Y., B. Yang, S. Wang, T. Jin, and S. Li, "An enhanced multi-objective grey wolf optimizer for service composition in cloud manufacturing," *Applied Soft Computing*, Vol. 87, 106003, Feb. 2020.

[26] Eappen, G. and T. Shankar, "Multi-objective modified grey wolf optimization algorithm for efficient spectrum sensing in the cognitive radio network," *Arabian Journal for Science and Engineering*, Vol. 46, No. 4, 3115–3145, 2021.